Publication Year	2018
Acceptance in OA	2020-10-26T16:40:12Z
Title	The ESO Multi-instrument Kinematic Survey (MIKiS) of Galactic Globular Clusters: Solid-body Rotation and Anomalous Velocity Dispersion Profile in NGC 5986
Authors	Lanzoni, B., Ferraro, F. R., Mucciarelli, A., Pallanca, C., Tiongco, M. A., Varri, A., Vesperini, E., BELLAZZINI, Michele, Dalessandro, Emanuele, ORIGLIA, Livia, Valenti, E., SOLLIMA, ANTONIO LUIGI, Lapenna, E., Beccari, G.
Publisher's version (DOI)	10.3847/1538-4357/aad810
Handle	http://hdl.handle.net/20.500.12386/28007
Journal	THE ASTROPHYSICAL JOURNAL
Volume	865

The ESO Multi-Instrument Kinematic Survey (MIKiS) of Galactic Globular Clusters: solid body rotation and anomalous velocity dispersion profile in NGC 5986[1]

B. Lanzoni[2,3], F. R. Ferraro[2,3], A. Mucciarelli[2,3], C. Pallanca[2,3], M. A. Tiongco[4], A. Varri[5], E. Vesperini[4], M. Bellazzini[3], E. Dalessandro[3], L. Origlia[3], E. Valenti[6], A. Sollima[3], E. Lapenna[2,3], G. Beccari[6]

[2] *Dipartimento di Fisica e Astronomia, Università degli Studi di Bologna, via Gobetti 93/2, I–40129 Bologna, Italy*

[3]*INAF-Osservatorio di Astrofisica e Scienza dello Spazio di Bologna, Via Gobetti 93/3, 40129, Bologna, Italy*

[4] *Department of Astronomy, Indiana University, Bloomington, IN, 47401, USA*

[6] *Institute for Astronomy, University of Edinburgh, Royal Observatory, Blackford Hill, Edinburgh EH9 3HJ, UK*

[6]*European Southern Observatory, Karl-Schwarzschild-Strasse 2, 85748 Garching bei München, Germany*

3 August 2018, ApJ in press

ABSTRACT

As part of the ESO-VLT Multi-Instrument Kinematic Survey (MIKiS) of Galactic globular clusters, we present a detailed investigation of the internal kinematics of NGC 5986. The analysis is based on about 300 individual radial velocities of stars located at various distances from the cluster center, up to $300''$ (about 4 half-mass radii). Our analysis reveals the presence of a solid-body rotation extending from the cluster center to the outermost regions probed by the data, and a velocity dispersion profile initially declining with the distance from the cluster's center, but flattening and staying constant at ~ 5 km s^{-1} for distances larger than about one half-mass radius. This is the first globular cluster for which evidence of the joint presence of solid-body rotation and flattening in the outer velocity dispersion profile is found. The combination of these two kinematical features provides a unique opportunity to shed light on fundamental aspects of globular cluster dynamics and probe the extent to which internal relaxation, star escape, angular momentum transport and loss, and the interaction with the Galaxy tidal field can affect a cluster's dynamical evolution and determine its current kinematical properties. We present the results of a series of N-body simulations illustrating the possible dynamical paths leading to kinematic features like those observed in this cluster and the fundamental dynamical processes that underpin them.

Subject headings: globular clusters: individual (NGC 5986); stars: kinematics and dynamics; techniques: spectroscopic

1. INTRODUCTION

The ESO-VLT Multi-Instrument Kinematic Survey (hereafter the MIKiS survey; Ferraro et al. 2018a) of Galactic globular clusters (GCs) is a project specifically designed to characterize the kinematical properties along the line-of-sight of an illustrative selection of GCs in the Milky Way. We have measured individual radial velocities (RVs) of hundreds of stars, distributed over the entire radial range of each stellar system. To this end, the survey fully exploits the spectroscopic capabilities of different instruments currently available at the ESO Very Large Telescope (VLT): the adaptive-optics assisted integral-field spectrograph SINFONI, the multi-object integral-field spectrograph KMOS, and the multi-object fiber-fed spectrograph FLAMES.

The evolutionary interplay between two-body relaxation-driven processes and the effects of the external tidal environment gives origin to a rich internal kinematics in collisional systems, which is now observationally accessible. Moreover, Milky Way GCs are very old stellar systems (with ages of $\sim$ 10 Gyr or more; see e.g. Forbes & Bridges 2010) orbiting the Galaxy since the remote epoch of its formation. Hence, signatures of such a long-term interaction could be present in their observational properties. In this context, both the inner and the outer portions of the kinematic profiles provide crucial information on the dynamics of the systems: for instance, a central gradient in the velocity dispersion profile could be used to constrain the presence of an intermediate-mass black hole; the external portion provides information on the possible tidal perturbations due to interaction of the cluster with the Galactic tidal field.

A growing set of observational evidence is indeed unveiling an unexpected dynamical complexity in Galactic GCs, demonstrating that the traditional assumptions of sphericity, pressure isotropy and non-rotation are far too simplistic (for references on morphological distortion, velocity anisotropy and rotation observed in Galactic GCs, see the comprehensive list reported in Ferraro et al. 2018a). In particular, Fabricius et al. (2014) detected signals of rotation in all the 11 Milky Way GCs studied in their survey and Kamann et al. (2018) found evidence of rotation in 60% of their sample (of 25 objects). In the context of the MIKiS survey, Ferraro et al. (2018a) recently found rotation signals at distances of a few half-mass radii from the center in 10 Milky Way GCs (out of 11 investigated) and Lanzoni et al. (2018) detected in M5 one of the cleanest and most coherent rotation patterns ever observed in a GC. All these results suggest that, when

---

[1] Based on FLAMES and KMOS observations performed at the European Southern Observatory as part of the Large Programme 193.D-0232 (PI: Ferraro).

properly studied, the vast majority of GCs shows signatures of the presence of internal rotation. According to a number of numerical studies (see e.g. Einsel & Spurzem 1999; Ernst et al. 2007; Tiongco et al. 2017), the present-day signatures could be the relic of a stronger internal rotation set at the epoch of the cluster's formation (see e.g., Vesperini et al. 2014; Lee & Hennebelle 2016; Mapelli 2017) and gradually altered and erased as result of the effects of angular momentum transfer and loss due to internal dynamical processes and star escape. In addition, as shown in the recent study by Tiongco et al. (2018), the interplay between internal dynamics and the interaction with the Galactic tidal field can produce a number of complex kinematical features in rotating clusters, including a radial variation in the orientation of the rotation axis: this would be the manifestation of the transition between the inner regions dominated by the cluster's intrinsic rotation, and the outer regions dominated by the rotation induced by the Galaxy tidal torque.

As part of the MIKiS survey, here we present the velocity dispersion and rotation profiles in the intermediate/outer regions of NGC 5986. This is a relatively poorly investigated Galactic GC (see Alves et al. 2001 and reference therein). It is massive (with total V-band magnitude $M_V = -8.44$) and of moderate concentration ($c = 1.23$), with core and projected half-light (or projected half-mass, at a first approximation) radii $r_c = 28.2''$ and $R_h = 58.8''$, respectively (Harris 1996) and with three-dimensional half-mass radius $r_h \sim 78.16''$, as obtained from the corresponding King (1966) model. Because of various physical properties in common with the group of "iron-complex" GCs (da Costa 2016), NGC 5986 was suspected to be the remnant of a disrupted dwarf galaxy. However, a recent high-resolution spectroscopic investigation of 25 giant stars (Johnson et al. 2017) provided accurate measure of the cluster metallicity ([Fe/H]$= -1.54$) and showed that it is homogeneous in iron and with a well defined anti-correlation between the Al and the Mg abundances, in agreement with what expected for genuine GCs.

The paper is structured as follows, In Section 2 we briefly summarize the observations, the adopted data reduction procedures, and the method used to measure the stellar RVs. The main results of our kinematic study are presented in Section 3: the cluster has been characterized in terms of its systemic velocity and the radial profiles of its ordered and disordered motions. Section 4 discusses the observational results in the context of recent N-body simulations of tidally perturbed clusters, illustrating three possible paths that could lead to the observed features.

2. Observations, data reduction and radial velocities

The observational strategy of the MIKiS survey and the adopted procedures to reduce the data are presented and discussed by Ferraro et al. (2018a,b, see also Lanzoni et al. 2018). In short, in the case of NGC 5986, we combined data acquired with FLAMES in the GIRAFFE/MEDUSA mode (using the HR21 grating, with resolving power R$\sim$ 16200 and spectral coverage 8484-9001 Å) and KMOS (with the YJ grating, covering 1.00-1.35 μm at a resolution R$\approx$3400). In particular, we secured five pointings with FLAMES (with integration times ranging from 2400 to 3500 s) and nine KMOS pointings (with integration times between 30 and 60 s). The spectroscopic targets have been selected from the HST-ACS catalog of Sarajedini et al. (2007), the 2MASS infrared catalog (Skrutskie et al. 2006) and ground-based wide-field observations. Particular care was devoted to select isolated targets with no bright contaminant neighbor within $2''$-$3''$. The usual pre-reduction process of the raw data was performed by using the standard pipelines.[2] In the case of KMOS, the RV of each target was measured from the spectrum manually extracted from the brightest spaxel of each stellar centroid.

RV measurements were obtained following the procedure already described in previous papers (see Ferraro et al. 2018a; Lanzoni et al. 2018). First, the observed spectra have been corrected for the heliocentric velocity, then cross-correlated with synthetic spectra of appropriate metallicity, spectral resolution and stellar parameters. An example of synthetic template, and RV-corrected observed spectrum for a KMOS and for a FLAMES target is shown in Figure 1. In the case of the FLAMES data, the cross-correlation procedure has been applied to patterns of absorption lines observed in three different wavelength ranges (see Ferraro et al. 2018a). For KMOS data, because of the lower spectral resolution, and the fact that fewer stellar absorptions and several telluric lines are present in the near-infrared spectral region, RVs have been determined from the cross-correlation with individual features.

For the spectra acquired with FLAMES, typical uncertainties in the RVs are of the order of 0.5 km s^{-1} and 1 km s^{-1} for the brightest ($V < 16.5$) and the faintest portion of the sample. These have been derived from the dispersion of the RV measures obtained from the considered spectral windows, and also comprise the uncertainty on the wavelength calibration. For KMOS, we first verified that no systematic RV offsets were present with respect to the FLAMES measures, by using a dozen of stars in common. Then, the RV errors have been estimated on the basis of the signal-to-noise ratios using the relation reported in Lanzoni et al. (2018).[3] For the stars measured with both the instruments, the RV determined from the FLAMES spectra has been adopted. The kinematic catalog of NGC 5986 is freely available at the MIKiS web page.[4]

3. Results

3.1. Systemic velocity

We illustrate in Figure 2 the radial distribution of the 470 line-of-sight velocities measured in this work. As value for the cluster center we adopted the one quoted in Goldsbury et al. (2011).

---

[2] http://www.eso.org/sci/software/pipelines/

[3] Note that in the case of NGC 5986, because of the low metallicity of the cluster, several spectra acquired with KMOS had signal-to-noise ratios smaller than 30. Hence, only stars with errors below to 9 km s^{-1}, with a mean value of 6.8 km s^{-1}, have been retained and used in the present analysis.

[4] http://www.cosmic-lab.eu/Cosmic-Lab/MIKiS_Survey.html

Although the surveyed stars are located out to $r = 760''$, cluster members appear to be distributed within $\sim 300''$ from the center and are all grouped around a mean velocity of ~ 100 km s^{-1}. The remaining objects clearly are Galactic field contaminants, showing a much broader RV distribution. To determine the cluster systemic velocity ($V_{\rm sys}$) we conservatively used only the sub-sample of (313) likely-member stars observed with FLAMES at $r < 300''$. After applying 3-σ rejection cleaning to this sample, we estimated $V_{\rm sys}$ by following the maximum-likelihood approach fully described in Section 3.4.1 of Walker et al. (2006, see also Martin et al. 2007; Sollima et al. 2009). Briefly, this consists in determining the values of the mean velocity and velocity dispersion that maximize the joint probability of having observed a given set of RVs, under the hypothesis that the measures have a Gaussian distribution (which is fully appropriate for this cluster; see Figure 2). By construction, this method also takes into account the error associated to each individual RV. To estimate the uncertainties on the two parameters, we have followed the classical approach outlined by Pryor & Meylan (1993). The mean velocity thus obtained, corresponding to the cluster systemic velocity, is $V_{\rm sys} = 100.8 \pm 0.3$ km s^{-1}. This is larger than the value quoted by Harris (1996, 2010 edition: $V_{\rm sys} = 88.9 \pm 3.7$ km s^{-1}), but in very good agreement with the recent estimate of Johnson et al. (2017, $V_{\rm sys} = 99.76$ km s^{-1}). In the following, we will denote as $V_r \equiv {\rm RV} - V_{\rm sys}$ the RVs to which the cluster systemic velocity has been subtracted. Figures 3 and 4 show the color-magnitude diagram and the distribution on the plane of the sky of the selected cluster members. As apparent, the KMOS targets are all bright giants ($V < 14.8$) mainly located in the cluster central region, while the stars surveyed with FLAMES are observed along both the red giant branch down to $V = 17.5$ and the horizontal branch, sampling both the center and the outskirts of the system.

3.2. Rotation curve and velocity dispersion profile

We searched for signatures of ordered motions in NGC 5986 following the same approach adopted in the previous papers of this series (Ferraro et al. 2018a; Lanzoni et al. 2018) and presented in full detail by, e.g., Bellazzini et al. (2012, see also Lanzoni et al. 2013). To define the position angle (PA) of the rotation axis we considered a line passing through the center of the system and dividing the observed RV sample in two portions. We then varied the PA of the line in the anti-clockwise direction from 0° (North) to 180° (South), at each step determining the difference $\Delta V_{\rm mean}$ between the average velocity of the RV samples on either sides of the line. Finally, we fitted the variation of $\Delta V_{\rm mean}$ as a function of PA with a sine function. In the presence of ordered motions, the rotation amplitude ($A_{\rm rot}$) is equal to half the maximum absolute value of the sine function, while the rotation axis position angle (PA$_0$) corresponds to the abscissa of the maximum. Moreover, the cumulative RV distributions of the samples located on either sides of the best-fit rotation axis, as well as the mean RV of the two sub-groups are expected to be different. Three indicators have thus been used to verify whether these differences are statistically significant: we evaluated the probability that the two RV distributions are extracted from the same parent family through a Kolmogorov-Smirnov test; we tested the hypothesis of different sample means through the Student's t-test and a maximum-likelihood approach.

By applying this procedure in distinct circular annuli around the cluster center, we found a significant signature at $r > 80''$ (see the top panels of Figure 5 and the values listed in the first row of Table 1). Indeed, all the three adopted estimators indicate that the detected rotation signal has high statistical significance: a Kolmogorov-Smirnov test returns a probability $P_{\rm KS} = 2.5 \times 10^{-3}$ that the two sub-samples are originated from the same parent distribution, following the Student's t-test, the probability that the means of the two samples are different is larger than 99.8% and, based on the maximum-likelihood approach, this difference is significant at 3.4 σ. If we apply the same procedure to the whole sample of stars (from $3''$ to $300''$) fixing the rotation axis at the best-fit position angle obtained for $r > 80''$ ($\rm PA_0 = 62°$), we find the results plotted in the bottom panels of Figure 5 and listed in the second row of Table 1. The significance of the global signal is weaker than that obtained for $r > 80''$ since the data considered for this calculation include the cluster's innermost regions where the strength of the rotation becomes increasingly smaller.

To determine the rotation curve of NGC 5986 we have first rotated the Cartesian coordinate system (x,y) over the position angle $\rm PA_0$. By construction, the resulting coordinate system (XR,YR) has the XR axis along the cluster major axis, and YR aligned with the rotation axis. We then applied the same maximum-likelihood method as above (Section 3.1) to determine the stellar mean velocity in five intervals of XR on both sides of the rotation axis. The rotation curve obtained through this procedure is plotted in Figure 6 and listed in Table 2. It shows a clear solid-body rotation pattern, monotonically increasing from 0 km $\rm s^{-1}$ in the center, up to ~ 2 km $\rm s^{-1}$ at the outermost sample distances, roughly corresponding to 4 half-mass radii. Its least square best-fit line has equation $V_{\rm rot} = a \times {\rm XR} + b$, where $a = 0.012$ km $\rm s^{-1}$ $\rm arcsec^{-1}$ and $b = -0.02$ km $\rm s^{-1}$, and high statistical significance, with a the Spearman rank correlation coefficient $\rho = 0.99$.

In principle, a non-negligible amount of the detected rotation could be due to the line-of-sight component of the cluster space motion (see, e.g., Feast et al. 1961). We thus checked the amplitude of the perspective rotation by following van de Ven et al. (2006). As systemic velocity we adopted the one determined in Section 3.1. For the systemic proper motion we used both the value quoted in Casetti-Dinescu et al. (2007) and the one recently measured from the second Gaia data release (Helmi et al. 2018). In both cases, we found that the cluster perspective rotation is negligible.

To determine the projected velocity dispersion profile $\sigma_p(r)$ of the cluster, we have first subtracted from each individual RV the mean rotational velocity at the position of the star. This removes the contribution of rotation to the second velocity moment, thus providing the "pure" velocity dispersion measure. Then, we applied the maximum-likelihood approach discussed above (Section 3.1) in six circular bins around the center of the system, and determined $\sigma_p(r)$ as the velocity dispersion value that maximizes the joint probability of having observed the set of RVs (and their associated errors) measured in that radial range. The resulting velocity dispersion profile is listed in Table 3 and plotted in Figure 7. As detailed in the table, the FLAMES measures (having errors of ~ 1 km $\rm s^{-1}$) always dominate the samples, both in the most central bin and, especially, in the outermost radial annuli (indeed, the obtained profile is perfectly consistent within the errors with that derived by using only the FLAMES measures). As apparent from the figure, after a decline between $0''$ and $\sim 90''$, the velocity dispersion stays approximately constant at ~ 5 km s^{-1} out to the outermost sampled radius.

4. Summary and Discussion

In this paper we presented a novel investigation of the internal kinematics of the Galactic GC NGC 5986, as based on hundred spectra of individual stars. We find one of the most significant rotation patterns hitherto detected in GCs (see also the cases of NGC 4372 in Kacharov et al. 2014, 47 Tucanae in Bellini et al. 2017, and M5 in Lanzoni et al. 2018), the only one so far showing a clear solid-body rotation behavior. For the first time, we also jointly find evidence of a velocity dispersion profile that flattens at distances larger than about one half-mass radius. The physical interpretation of the co-existence of these kinematic features requires particular care, because several dynamical pathways may be envisaged as a possible origin of the observed behaviors. A qualitative discussion of three possible channels, as based on recent theoretical investigations into the kinematic evolution of collisional stellar systems, is provided below.

One possibility is that such kinematic properties result from the evolution of the cluster in an external tidal field, with attention to the role played by a population of energetically unbound stars confined within the critical equipotential surface ("potential escapers"; see Heggie 2001). Recent studies based on direct N-body simulations have shown that such a population determines a flattening of the velocity dispersion profile in the outer regions of a stellar system (Küpper et al. 2010; Claydon et al. 2017). In addition, tidally perturbed clusters, during the course of their dynamical evolution (and irrespectively of their initial conditions), tend to develop a signature of solid-body rotation which depends on their orbital angular velocity partial synchronization (see Tiongco et al. 2016b; Claydon et al. 2017) and a degree of anisotropy which depends on their initial filling factor (e.g., see Giersz & Heggie 1997; Tiongco et al. 2016a). As a representative example of such an evolutionary behaviour, we illustrate the rotation curve and velocity dispersion profile of an N-body model originally presented by Tiongco et al. (2016b), depicted a different times (see Figure 8, first row). Such an N-body simulation starts from initial conditions sampled from a King (1966) equilibrium model, which is initially non-rotating, and is evolved on a circular orbit in the tidal field of a Keplerian potential (with an initial ratio of the intrinsic half-mass radius to the Jacobi radius given by $r_h/r_J = 0.087$). As apparent from the figure, the system progressively develops a solid-body rotation curve with an angular velocity consistent with $\Omega/2$ (where Ω denotes the orbital angular velocity; for further details, see model KF075U in Tiongco et al. 2016b). The corresponding velocity dispersion profiles progressively flatten in the outermost regions of the system (see right-hand panels).

A second pathway corresponds to the case of a collisional system which is initially characterized by some intrinsic internal rotation and is progressively evolving towards a condition of solid-body rotation (starting from its central to intermediate regions), as a result of the angular momentum transport and loss, induced by two-body relaxation processes. Such a case is exemplified by an

N-body model originally presented by Tiongco et al. (2016a), for which we again illustrate the evolution of the rotation curve and velocity dispersion profile at different times (see Figure 8, second row). The simulation starts from initial conditions sampled from differentially rotating equilibrium models (Varri & Bertin 2012) and includes the effect of a mild tidal field (corresponding to an initial ratio of the intrinsic half-mass radius to the Jacobi radius $r_h/r_J = 0.093$) associated to a circular orbit in a Keplerian galactic potential (for further details, see model VBrotF04 in Tiongco et al. 2016a). In this case, the evolution of the central slope value of the rotation curve is not determined by the influence of the tidal environment. In the represented model, only at a very late stage of evolution the rotation curve settles, as in the previous case, into a solid body-like behavior, with an angular velocity determined by the condition of partial synchronization. We wish to note that, in this pathway, the orientation of the axis of the initial intrinsic rotation, in principle, may also be different from the orientation of the orbital rotation axis (see Tiongco et al. 2018). As a result, a radial variation of the kinematic position angle may be found (e.g., see Bianchini et al. 2013; Boberg et al. 2017), which is not observed in the range explored in the current kinematic study.

An additional possible dynamical path is that of a stellar system experiencing a phase of “violent relaxation” in the presence of an external tidal field; in this case the violent relaxation process and the effects of the tidal field leave a distinctive fingerprint on the cluster’s internal kinematics from the very early stages of its evolution (see Vesperini et al. 2014), with a solid-body like behavior of the central portion of the rotation curve. Also in this case, the differential rotation imprinted during the early evolutionary stages progressively evolves towards the condition of partial synchronization described in the two previous cases. This third case is exemplified by a model originally presented by Tiongco et al. (2016a) and subsequently studied by Tiongco et al. (2017, see model vrQ01F05 for further details). The element of interest in this third case (see Figure 8, third row) mostly concerns the velocity dispersion profile, which becomes more flattened and extended at earlier times compared to the previous two cases. Such a difference is due to the fact that this model develops the population of energetically unbound stars responsible for the flattening of the velocity dispersion during the early violent relaxation phase.

The models shown in Figure 8 serve as a framework for a general interpretation of the observed features, but are not designed to provide a detailed and quantitative fit to the kinematical properties of NGC 5986. In particular we note that the flattening in the velocity dispersion observed in NGC 5986 is more extreme and internal than that found in all our models. As shown in several studies (see Casetti-Dinescu et al. 2007; Allen et al. 2008; Moreno et al. 2014), NGC 5986 is on an eccentric orbit and specific models for this cluster need to take into account the effects on the velocity dispersion due to the time variation in the strength of the external tidal field (see, e.g., Küpper et al. 2010). Indeed, a time-variable tidal field, as experienced by a star cluster moving on an elliptic orbit, has direct implications on the properties and time evolution of the population of potential escapers dynamically generated in a collisional stellar system, which, in turn, has an impact on the shape of its outer velocity dispersion profile (see especially Figure 3 in Küpper et al. 2010, and also Drukier et al. 2007; Claydon et al. 2017). We estimated the orbital parameters of the system in the Johnston et al. (1995) Milky Way potential well, adopting $V_{\rm sys} = 100.8$ km s^{-1} as systemic line-of-sight velocity (see Section 3.1) and the proper motions of Casetti-Dinescu et al. (2007) for the two components on the plane of the sky. We found that the system has a highly eccentric orbit ($e = 0.80$), practically plunging into the central part of the Milky Way along a path that is confined within the innermost few kpc from the Galactic center, with a pericentric distance $r_p = 0.5$ kpc and the apocenter at $r_a = 5.4$ kpc. These values are in very good agreement with those determined by Casetti-Dinescu et al. (2007), who used only a slightly smaller value of the systemic velocity. The orbital parameters estimated by Helmi et al. (2018) from the proper motions presented in the second Gaia data release also suggest that this cluster is on a very eccentric orbit with a very small pericentric distance: depending on the model adopted for the Galactic potential, the eccentricity is equal to 0.7, 0.81 or 0.87, while r_p varies between 0.85, 0.52 and 0.07 kpc, respectively. The orbital parameters derived for NGC 5986 thus suggest quite intense interactions with the central regions of the Galaxy, with an orbital radial period of only ~ 60 Myr, corresponding to a few hundreds passages of the cluster close to the Galactic center during its lifetime ($t = 12$ Gyr; Forbes & Bridges 2010). Thus, the effect of the time variation in the external tidal field is certainly playing an important role in the dynamics of NGC 5986 and must be included in simulations aimed at providing a detailed fit of the observed properties of this cluster. We point out here that, if the solid-body rotation revealed by our observations is the result of the cluster's convergence toward a state of partial synchronization with angular velocity $\Omega/2$, the angular velocity measured for NGC 5986 would correspond to the value of $\Omega/2$ at about 0.46 kpc (simply calculated assuming a circular velocity equal to 220 km/s).

To provide a comprehensive dynamical interpretation of this cluster some additional pieces of information are needed. First of all, the line-of-sight kinematics should be assessed also in the outer regions of the cluster, in the proximity (and ideally beyond) the nominal Jacobi radius. Indeed, the shape of the outer rotation curve is crucial to test the applicability of the three pathways described above. We also plan to search for density distortion or streams associated with tidal perturbations. In principle, crucial information will also be added by the stellar proper motions measured by Gaia that, once combined with the line-of-sight kinematics, would allow us to reconstruct the full three-dimensional structure of the velocity space of the system. We have already started to analyze the most recent Gaia data (see, e.g., Helmi et al. 2018), but this study is particularly challenging for NGC 5986 because of its relatively large distance from Earth (10.4 kpc; Harris 1996), the high level of Galactic contamination in the cluster's direction on the sky, and the fact that the cluster proper motion is almost indistinguishable from that of the bulge. From the theoretical point of view, we plan to construct dynamical models and N-body simulations specifically tailored to the case of NGC 5986, exploring, in particular, the effects of an external tidal field in the case of highly eccentric orbits repeatedly crossing the innermost region of the Galaxy. Such a comprehensive investigation is particularly timely, in light of the growing interest for the physical understanding of the morphological and dynamical properties of the peripheries of Galactic GCs, especially regarding the interpretation of the kinematic properties of possible "extra-tidal" structures.

FRF acknowledges the ESO Visitor Programme for the support and the warm hospitality at the ESO Headquarter in Garching (Germany) during the period when part of this work was performed.

REFERENCES

Allen, C., Moreno, E., & Pichardo, B. 2008, ApJ, 674, 237-246

Alves, D. R., Bond, H. E., & Onken, C. 2001, AJ, 121, 318

Bellazzini, M., Bragaglia, A., Carretta, E., et al. 2012, A&A, 538, A18

Bellini, A., Bianchini, P., Varri, A. L., et al. 2017, ApJ, 844, 167

Bianchini, P., Varri, A. L., Bertin, G., & Zocchi, A. 2013, ApJ, 772, 67

Boberg, O. M., Vesperini, E., Friel, E. D., Tiongco, M. A., & Varri, A. L. 2017, ApJ, 841, 114

Casetti-Dinescu, D. I., Girard, T. M., Herrera, D., et al. 2007, AJ, 134, 195

Claydon, I., Gieles, M., & Zocchi, A. 2017, MNRAS, 466, 3937

da Costa, G. S. 2016, The General Assembly of Galaxy Halos: Structure, Origin and Evolution, 317, 110

Drukier, G. A., Cohn, H. N., Lugger, P. M., et al. 2007, AJ, 133, 1041

Einsel, C., & Spurzem, R. 1999, MNRAS, 302, 81

Ernst, A., Glaschke, P., Fiestas, J., Just, A., & Spurzem, R. 2007, MNRAS, 377, 465

Fabricius M. H. et al., 2014, ApJ, 787, L26

Feast, M. W., Thackeray, A. D., & Wesselink, A. J. 1961, MNRAS, 122, 433

Ferraro, F. R., Mucciarelli, A., Lanzoni, B., et al. 2018a, ApJ, 860, 50

Ferraro, F. R., Mucciarelli, A., Lanzoni, B., et al. 2018b, The Messenger, 172, 18

Forbes, D., Bridges, T., 2010, MNRAS, 404, 1203

Giersz, M., & Heggie, D. C. 1997, MNRAS, 286, 709

Goldsbury, R., Richer, H. B., Anderson, J., et al. 2011, AJ, 142, 66

Harris, W. E. 1996, AJ, 112, 1487, 2010 edition

Heggie, D. C. 2001, Dynamics of Star Clusters and the Milky Way, 228, 29

Helmi A., et al., 2018, arXiv180409381

Jeffreson, S. M. R., Sanders, J. L., Evans, N. W., et al. 2017, MNRAS, 469, 4740

Johnson, C. I., Caldwell, N., Rich, R. M., et al. 2017, ApJ, 842, 24

Johnston, K. V., Spergel, D. N., & Hernquist, L. 1995, ApJ, 451, 598

Kacharov, N., Bianchini, P., Koch, A., et al. 2014, A&A, 567, A69

Kamann, S., Husser, T.-O., Dreizler, S., et al. 2018, MNRAS, 473, 5591

King I.R., 1966, AJ, 71, 64

Küpper, A. H. W., Kroupa, P., Baumgardt, H., & Heggie, D. C. 2010, MNRAS, 407, 2241

Lanzoni, B., Mucciarelli, A., Origlia, L., et al. 2013, ApJ, 769, 107

Lanzoni, B., Ferraro, F. R., Mucciarelli, A., et al. 2018, ApJ, in press

Lee, Y.-N., & Hennebelle, P. 2016, A&A, 591, A31

Mapelli, M. 2017, MNRAS, 467, 3255

Martin, N. F., Ibata, R. A., Chapman, S. C., Irwin, M., & Lewis, G. F. 2007, MNRAS, 380, 281

Moreno, E., Pichardo, B., & Velázquez, H. 2014, ApJ, 793, 110

Pryor, C., & Meylan, G. 1993, Structure and Dynamics of Globular Clusters, 50, 357

Sarajedini, A., Bedin, L. R., Chaboyer, B., et al. 2007, AJ, 133, 1658

Sollima, A., Bellazzini, M., Smart, R. L., et al. 2009, MNRAS, 396, 2183

Skrutskie, M. F., Cutri, R. M., Stiening, R., et al. 2006, AJ, 131, 1163

Tiongco, M. A., Vesperini, E., & Varri, A. L. 2016a, MNRAS, 455, 3693

Tiongco, M. A., Vesperini, E., & Varri, A. L. 2016b, MNRAS, 461, 402

Tiongco, M. A., Vesperini, E., & Varri, A. L. 2017, MNRAS, 469, 683

Tiongco, M. A., Vesperini, E., & Varri, A. L. 2018, MNRAS, 475, L86

van de Ven, G., van den Bosch, R. C. E., Verolme, E. K., & de Zeeuw, P. T. 2006, A&A, 445, 513

Varri, A. L., & Bertin, G. 2012, A&A, 540, A94

Vesperini, E., Varri, A. L., McMillan, S. L. W., & Zepf, S. E. 2014, MNRAS, 443, L79

Walker, M. G., Mateo, M., Olszewski, E. W., et al. 2006, AJ, 131, 2114

This preprint was prepared with the AAS LaTeX macros v5.2.

Table 1: Rotation Signatures in NGC 5986

r_i	r_e	r_m	N	PA$_0$	$A_{\rm rot}$	$P_{\rm KS}$	$P_{\rm Stud}$	n-$\sigma_{\rm ML}$
80	301	149.5	209	62	1.4	2.5×10^{-3}	> 99.8	3.4
3	301	107.7	358	62	0.7	7.7×10^{-2}	> 90.0	2.2

Note. — Rotation signatures detected at $r > 80''$ (first row) and over the entire radial range surveyed by the observations (second row). Starting from the left: inner (r_i) and outer (r_e) radius of the considered radial interval (arcseconds), mean distance from the center of the stars in the annulus (r_m), star number (N), position angle of the rotation axis (PA$_0$, in degrees), rotation amplitude of the best fitting sinusoidal function (A$_{\rm rot}$, in km s^{-1}; see Fig. 5), probability outcome of the KS test ($P_{\rm KS}$) and of the t-Student test ($P_{\rm Stud}$), significance (n-$\sigma_{\rm ML}$) of the difference of the two means according to a maximum-likelihood approach (units of n-σ).

Table 2: Rotation Curve of NGC 5986

XR$_i$	XR$_e$	XR$_m$+	N+	$V_{\rm rot}$+	ϵ_{V+}	XR$_m-$	$N-$	$V_{\rm rot}-$	ϵ_{V-}
1	30	14.5	51	0.0	0.9	-16.1	56	-0.4	0.9
30	60	44.4	45	0.2	1.0	-44.9	41	-0.4	1.0
60	90	76.7	32	0.8	1.0	-76.0	26	-0.6	1.0
90	130	107.9	27	1.4	1.2	-109.2	25	-1.4	1.4
130	310	186.1	25	2.4	0.9	-183.8	26	-2.2	1.0

Note. — Rotation curve of NGC 5986 in a coordinate system (XR, YR) where the vertical axis is oriented as the rotation axis and points toward the North-East direction, while XR points toward North-West. The first two columns report the inner (XR$_i$) and outer (XR$_e$) boundaries (arcseconds) of the five considered bins. Columns 3-6 list, for the positive side of the XR axis, the mean cluster-centric distance (XR$_m$+) of the stars in each bin, their number (N+), and their average velocity and associated error in km s^{-1} ($V_{\rm rot}$+ and ϵ_{V+}+, respectively). The quantities reported in columns 7-10 are equivalent to those of 3-6, for the bins in the negative side of the XR axis.

Table 3: Projected Velocity Dispersion Profile of NGC 5986

r_i	r_e	r_m	N	N_K	N_F	σ_P	ϵ_σ
3	44	29.0	61	23	38	7.4	0.8
44	70	57.6	60	10	50	6.5	0.7
70	94	81.3	59	7	52	4.8	0.5
94	127	110.3	61	3	58	5.3	0.5
127	180	149.5	59	1	58	5.3	0.5
180	301	226.0	57	1	56	5.4	0.5

Note. — Projected velocity dispersion profile of NGC 5986, calculated in circular annuli around the center of the cluster. Starting from the left, the columns report: internal (r_i) and external (r_e) boundaries of the annuli (arcseconds), average cluster-centric position of the stars belonging to the bin (r_m), total number of stars (N), number of KMOS and FLAMES targets (N_K and N_F, respectively), projected velocity dispersion (σ_P) and associated error (ϵ_σ), in km s^{-1}.

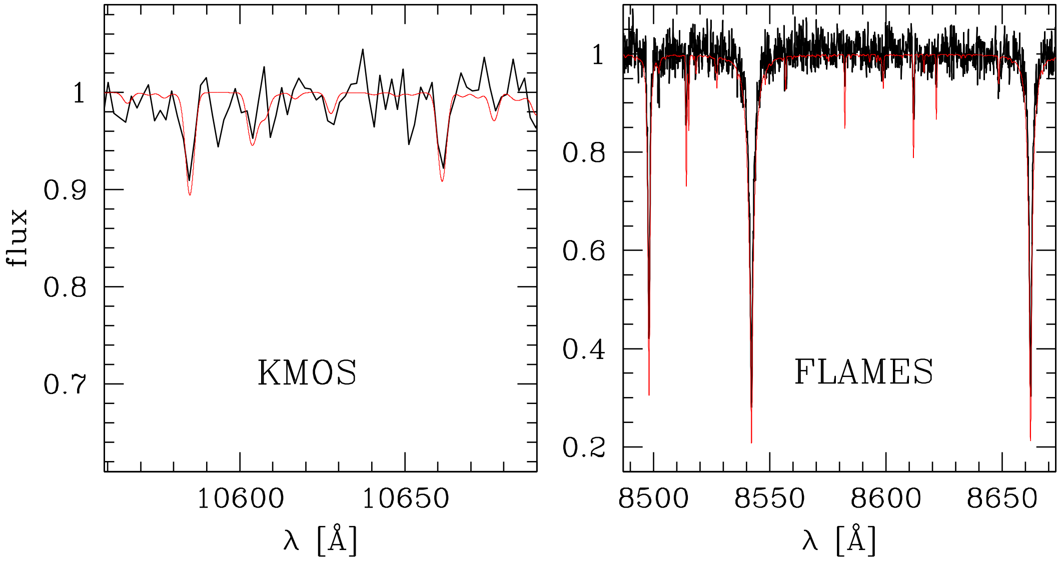

Fig. 1.— Examples of KMOS (left) and FLAMES (right) spectra. The observatons are plotted in black, while the synthetic templates are in red. Fluxes are arbitrarily normalized to unit.

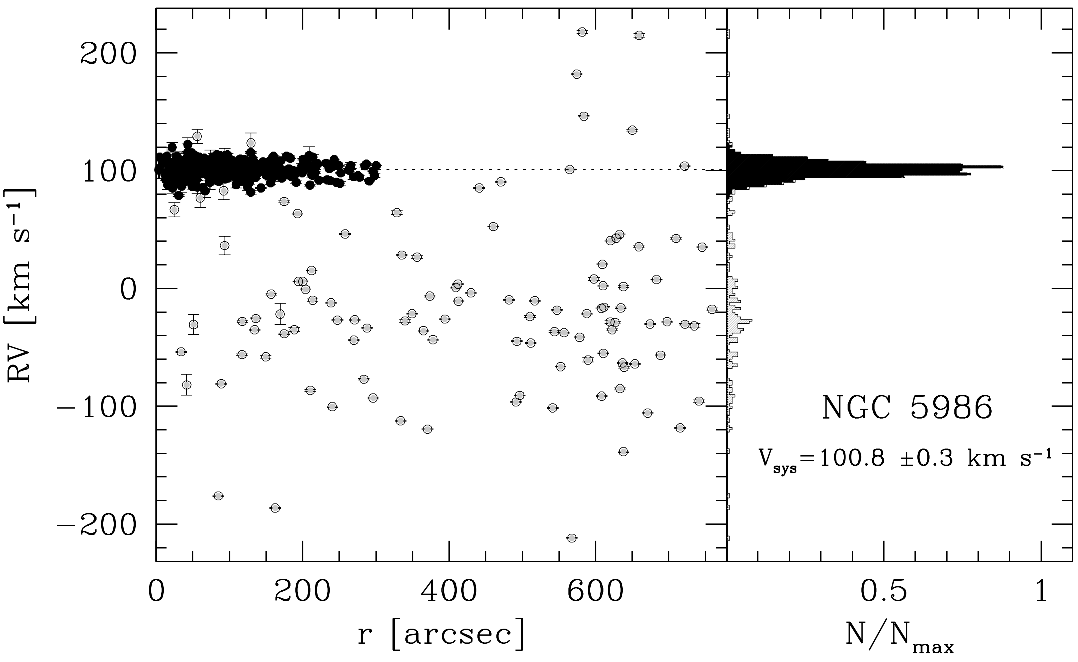

Fig. 2.— *Left panel:* Radial distribution of the line-of-sight velocities measured from the MIKiS observations in NGC 5986. The selected cluster members are plotted as black circles, while field contaminants are in grey. *Right panel:* RV distribution as a normalized histogram. $V_{\rm sys}$ denotes the cluster systemic velocity.

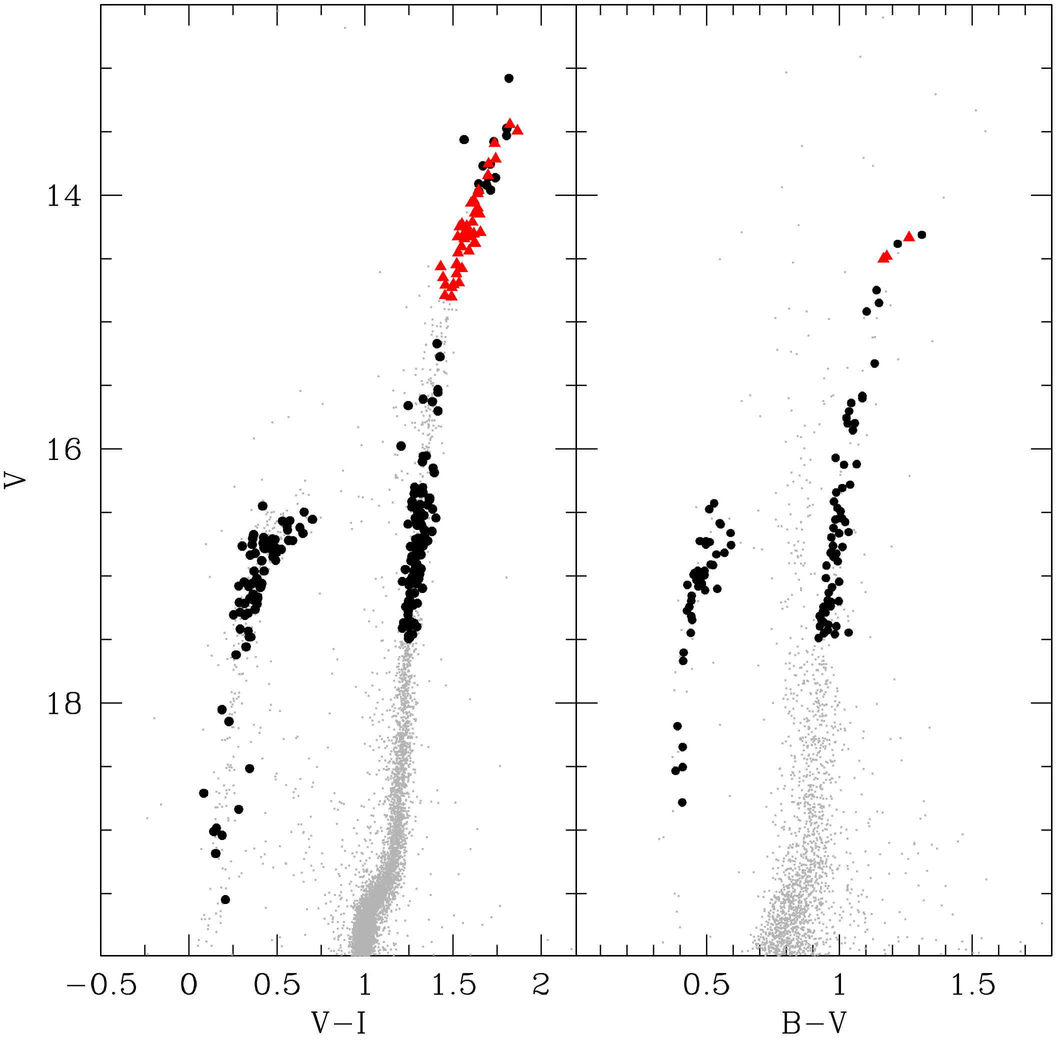

Fig. 3.— Position of the surveyed kinematic members in the color-magnitude diagrams of NGC 5986. The KMOS targets are highlighted as red triangles, while the stars surveyed with FLAMES are plotted as black circles.

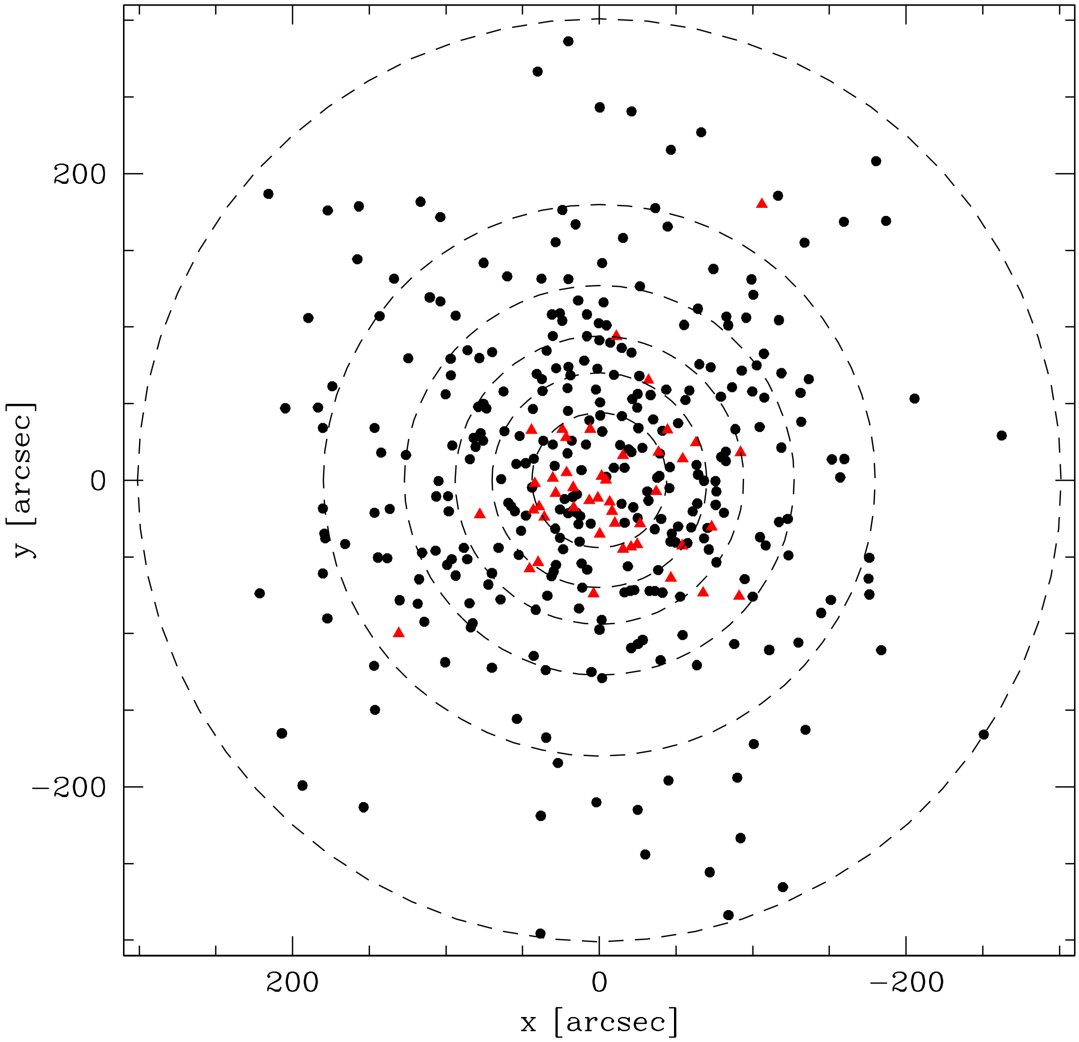

Fig. 4.— Position the surveyed kinematic members in the plane of the sky. Symbols have the same meaning as in Figure 3. The plotted coordinates, x and y, are the right ascension and declination relative to the cluster center, determined by using equation (1) in van de Ven et al. (2006). The dashed circles mark the boundaries of the radial bins used to determine the cluster velocity dispersion (see Table 3).

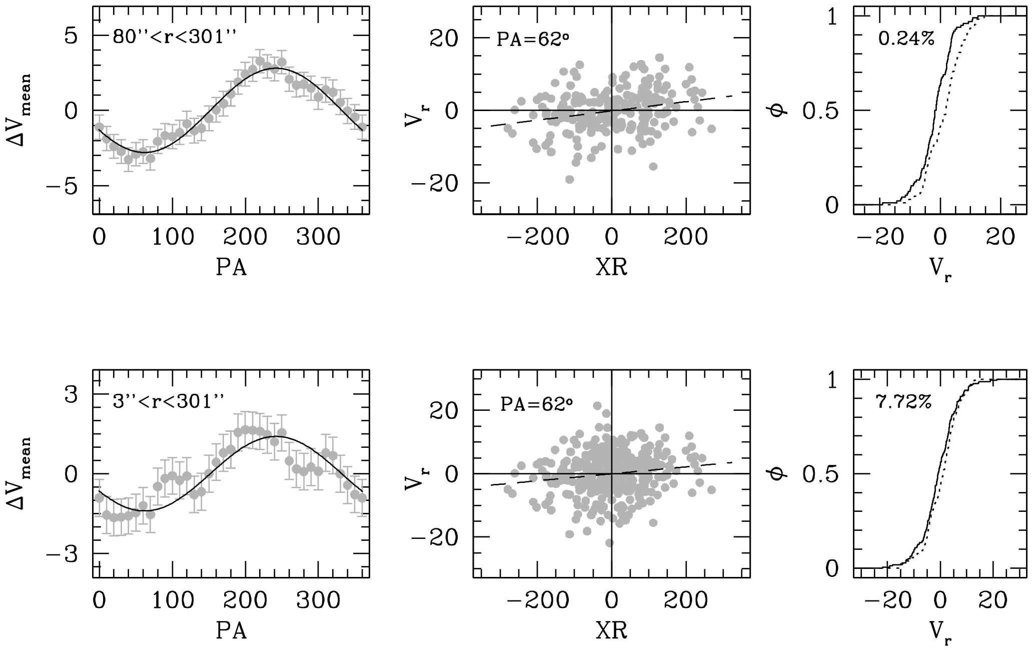

Fig. 5.— Diagnostic diagrams (see Section 3.2) of the rotation signatures detected at $r > 80''$ (upper row) and over the entire radial range surveyed (lower row). *Left panels:* difference between the mean line-of-sight velocity calculated in the two half-planes, as a function of the position angle of the dividing line. The labels indicate the radial range considered. *Central panels:* spatial distribution of the radial velocities (in km s^{-1}). XR denotes the projected distance from the best-fit rotation axis (in arcsec), with the value of the position angle marked. *Right panels:* cumulative distribution of the RVs with positive (dotted line) and negative (solid line) projected distance XR. The outcome of a KS test of the two distributions is reported in the top left corner of each panel.

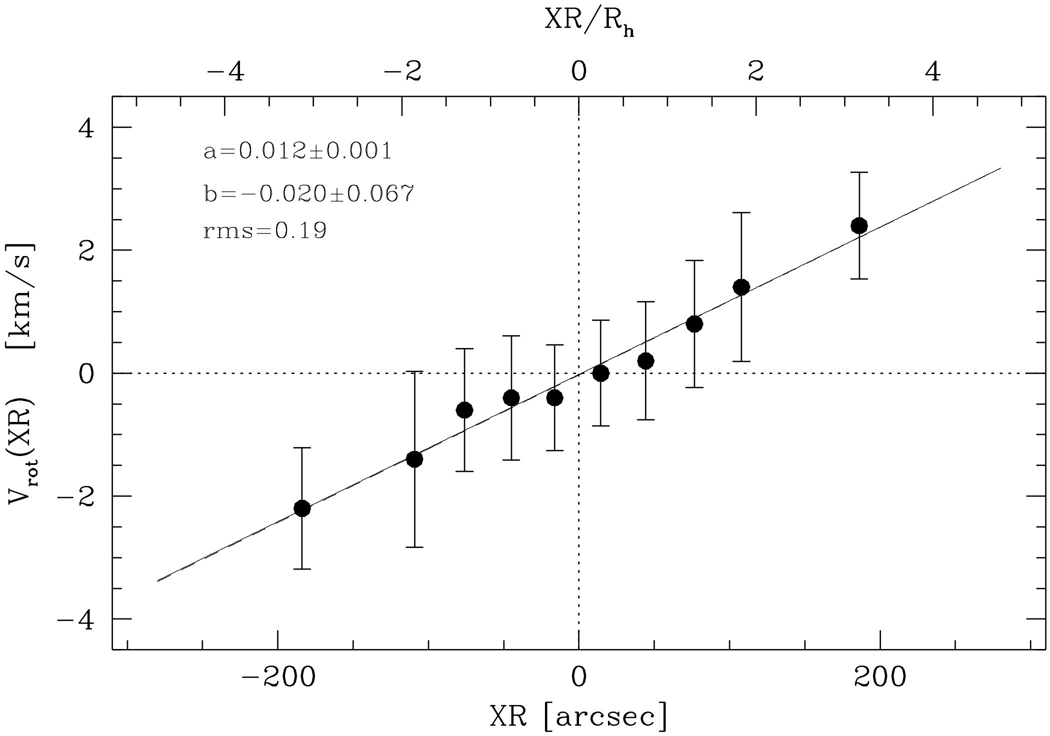

Fig. 6.— Rotation curve of NGC 5986. The mean velocity as a function of the distance from the rotation axis is displayed (see also Table 2). The best-fit line to the observed behavior has slope (*a*), intercept (*b*) and rms scatter (rms) as labelled in the figure.

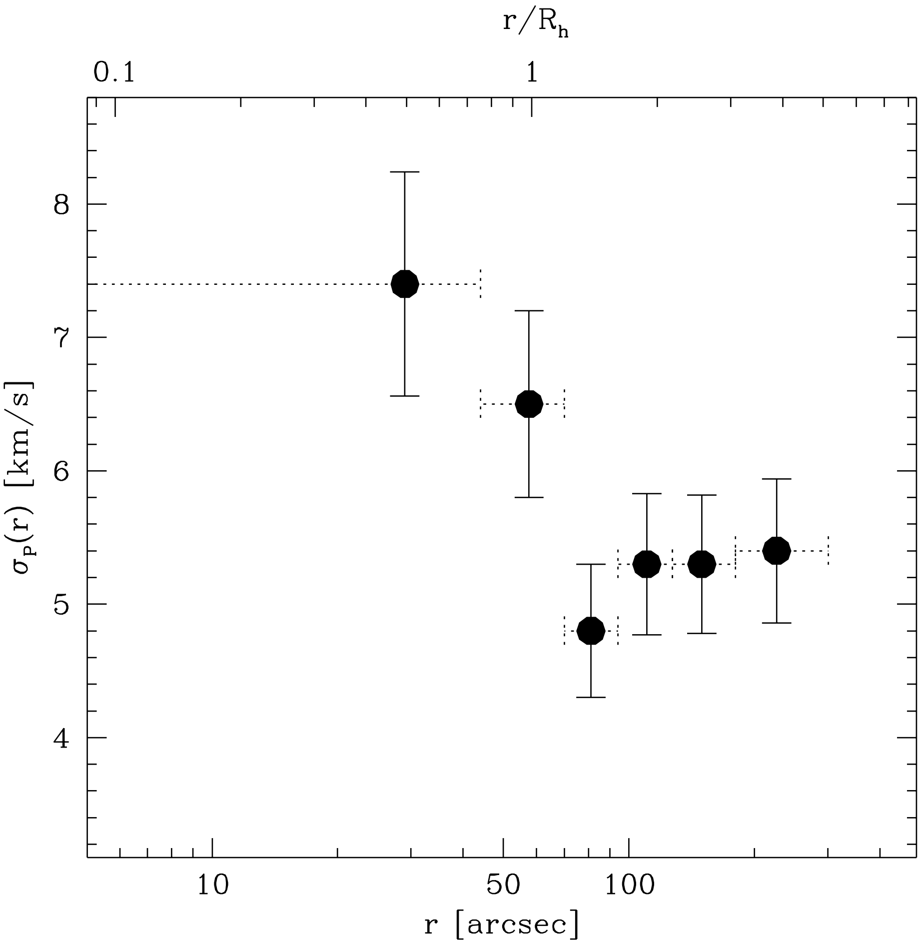

Fig. 7.— Projected velocity dispersion profile, determined after subtraction of the rotational contribution to the individual RVs, in six concentric annuli around the cluster center.

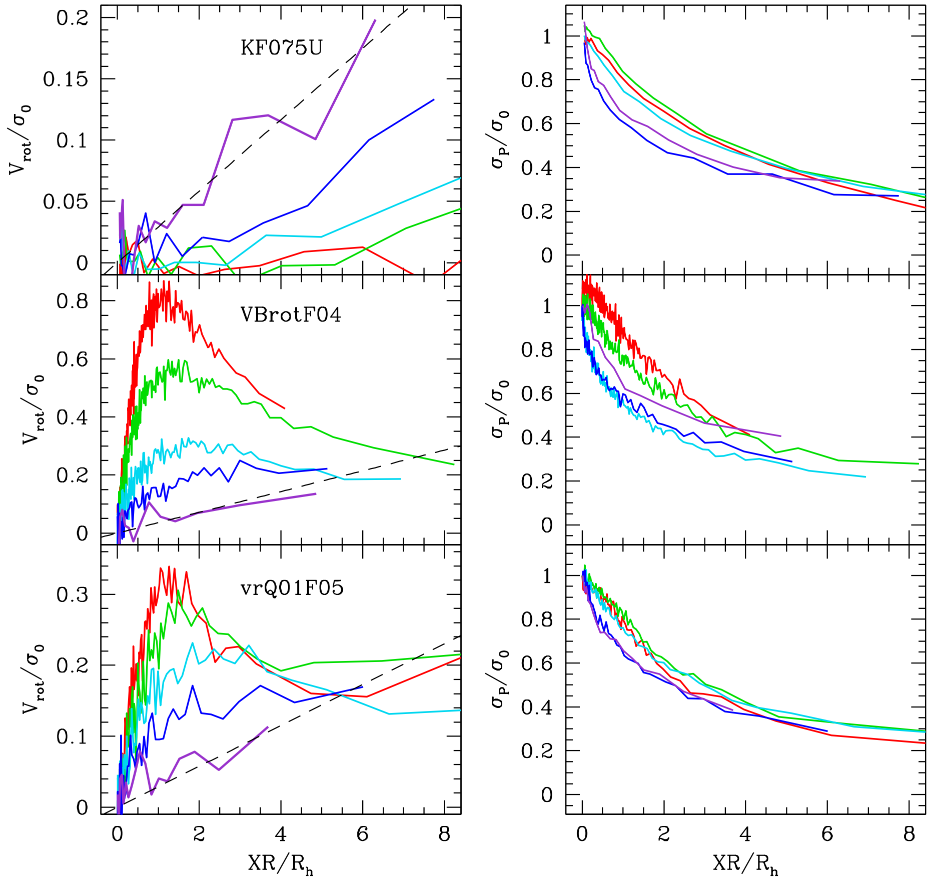

Fig. 8.— Time evolution of the rotation curve (left-hand panels) and velocity dispersion profile (right-hand panels), both calculated from line-of-sight velocities and normalized to the central velocity dispersion, for three of the N-body simulations from Tiongco et al. (2016a). The radius is normalized to the projected half-mass radius, R_{h}. Different lines correspond to different dynamical stages, with the red, green, cyan, blue and purple lines corresponding to increasing dynamical ages. In the left panels, a dashed line shows a theoretical solid-body rotation curve with slope $\Omega/2$, a value that star clusters will converge to during their long-term evolution in a tidal field (see Tiongco et al. 2016b). In all cases, both sets of kinematic profiles have been calculated by considering all stars enclosed within one Jacobi radius.